

Ultra-Broadband High-Efficiency Airy Optical Beams Generated with All-Silicon Metasurfaces

Ze Zhao Ju, Jing Wen, Lina Shi, Binbin Yu, Ming Deng, Dawei Zhang,* Weiming Hao, Jian Wang, Shuqi Chen, and Lin Chen*

Conventional approaches for generating Airy beams rely upon bulky and costly systems, which impede the miniaturization of optical systems. Metasurfaces have provided a compact method to generate Airy optical beams, but the current schemes suffer from the issues of narrow bandwidths and/or low transmission efficiencies. Here, a design strategy of constructing broadband and high-efficiency transmissive Airy optical beam generator by taking advantages of the high birefringence and transmission efficiency of dielectric metasurfaces is proposed. The local amplitude and phase of transmitted light can be simultaneously modulated to satisfy the Airy function by controlling the orientation angles of silicon nano-pillars, regardless of the incidence wavelength. The resultant Airy beam generator is experimentally verified within an ultra-wide operation bandwidth from 1.1 to 1.7 μm . The remarkable diffraction-free, self-accelerating, and self-healing properties of Airy beams are also demonstrated. The results may power up viable opportunities for practical devices and applications of metasurface-based Airy beams.

a wide range of applications including optical micromanipulation,^[1,2] chip-scaled signal processing,^[3,4] microscopy,^[5,6] generation of curved plasma channels,^[7] light bullet,^[8,9] and vacuum electron acceleration.^[10,11] For generating Airy optical beams, it is highly desirable to precisely control light waves to satisfy the amplitude and phase distributions described by Airy function. Conventional protocols for generating Airy beams rely on the utilization of bulky optical elements, such as spatial light modulators (SLMs),^[5,9,12,13] liquid crystals (LCs),^[14–16] lens,^[17] and phase plate.^[18,19] These schemes suffer from low transmission efficiencies with SLMs or LCs (typically less than 40%), and long device lengths with lens and phase plates.^[16–20]

Metasurfaces provide an unprecedented approach to control light waves in terms of amplitude, phase, polarization, and so

1. Introduction

As one type of non-diffraction beams, Airy beams have received enormous interest due to the unique diffraction-free, self-accelerating, and self-healing properties. Airy beams have found


on. The past few years have witnessed the rapid development of optical functional devices and applications with metasurfaces, including polarization control,^[21–24] flat lens,^[25–30] holographic imaging,^[31–33] invisibility cloaks,^[34,35] and orbital angular momentum.^[36–39] Different from phase-only modulation optical elements and applications, such as lens or holograms, the implementation of Airy beams requires simultaneous amplitude and phase modulation. Recently, metasurfaces offered a compact method to build Airy beam generators due to their great capability to manipulate light waves. Many metasurface configurations, including plasmonic metasurfaces,^[40–45] dielectric nano-rods,^[46–48] and hyperbolic metamaterials^[49] have been developed for Airy beam generation in the past few years. However, most of these schemes use some resonant building blocks to modulate light waves across the resonant frequencies; the resultant phase and amplitude profiles no longer abide by the Airy function out of the resonant frequencies. Consequently, the Airy beams can only be realized within a rather narrow bandwidth around the resonant frequencies. Some efforts have been dedicated to broadening the working bandwidth, but the transmission efficiencies are reduced significantly once the working frequencies deviate from the resonant frequencies.^[42,45] The recently reported dielectric metasurfaces have provided a robust approach to increase the transmission efficiency, however, these schemes are purposely designed to enable phase modulation, resulting in low quality of the generated beams due to lack of amplitude modulation.^[46–48] Broadband high-efficiency Airy beams have been proposed and experimentally demonstrated

Z. Ju, M. Deng, W. Hao, Prof. J. Wang, Prof. L. Chen
Wuhan National Laboratory for Optoelectronics
Huazhong University of Science and Technology
Wuhan 430074, China
E-mail: chen.lin@mail.hust.edu.cn

Prof. J. Wen, B. Yu, Prof. D. Zhang
Engineering Research Center of Optical Instrument and System
Ministry of Education and Shanghai Key Laboratory of Modern
Optical System
University of Shanghai for Science and Technology
Shanghai 200093, China
E-mail: dwzhang@usst.edu.cn

Dr. L. Shi
Key Laboratory of Microelectronic Devices and Integrated Technology
Institute of Microelectronics
Chinese Academy of Sciences
Beijing 100029, China

Prof. S. Chen
The MOE Key Laboratory of Weak Light Nonlinear Photonics
School of Physics and TEDA Institute of Applied Physics
Nankai University
Tianjin 300071, China

 The ORCID identification number(s) for the author(s) of this article can be found under <https://doi.org/10.1002/adom.202001284>.

DOI: 10.1002/adom.202001284

at microwave frequencies by use of hyperbolic metamaterials comprised of metal/dielectric multilayer.^[49] While such a scheme is applicable to optical frequencies by scaling down the structures in principle, the inherent ohmic loss will deteriorate efficiency of the Airy beams. In addition, preparation of metal/dielectric multilayer and formation of vertical sidewall are challenging and costly issues in practice.

In this paper, we propose a design strategy of generating ultra-broadband high-efficiency Airy beams with all-dielectric metasurfaces, without dependence of the incident wavelength in principle. By utilization of silicon nano-pillars as the building blocks, we derive a criterion under which both the amplitude and phase distributions can be adjusted to follow the multivariate amplitude and binary phase profiles required by Airy function, regardless of the incident wavelength. Thanks to the high birefringence and transmission efficiencies over a wide spectral range with silicon metasurfaces, the co-designed Airy beam generator presents ultra-wide operation bandwidth and high transmission efficiencies, as validated by the optical experiment at telecommunication wavelengths.

2. Results and Discussions

2.1. Operating Principle

Figure 1 schematically shows the proposed Airy beam generator, consisting of silicon pillars on a silicon substrate. The side- and top- views of the subunit are presented in Figures 1a and 1b, respectively. We denote the three orthometric edges of the silicon pillar as length (l), width (w), and height (h). The silicon pillar has a length L , a width W , and a height H , along l , w , and h axes, respectively, and the transversal periods along the x - and y -directions are set as $P = P_x = P_y = 0.6 \mu\text{m}$. The silicon pillar exhibits birefringence because different polarizations have different mode indices once light waves are coupled. Consequently, the phase difference accumulated between the l - and w -polarizations can be modulated by the pillar geometry. It is worth emphasizing here, the silicon pillar can guide light waves regardless of the wavelength in principle, which is a prerequisite to design an Airy beam generator over a wide spectral band.

We now show how the silicon pillar works for constructing a transmissive Airy beam generator. When l - and w -polarized plane waves illuminate the subunit, the complex transmission coefficients, t_l and t_w , can be written as

$$t_l = A_l e^{i\varphi_l}, \quad t_w = A_w e^{i\varphi_w} \quad (1)$$

where A_l (A_w) and φ_l (φ_w), respectively, represent the transmission amplitude and phase along the l (w) polarization direction. The complex transmission coefficient for the l (w) polarization direction can be flexibly tuned by varying L and W . Consider a beam of x - polarized light waves, in which the electric field is represented by $\mathbf{E}_i = E_i \cdot \mathbf{x}$, with E_i and \mathbf{x} being of the amplitude and the unit vector along the x -direction, respectively. Once such a beam is normally illuminated on the subunit, the y -component of the transmitted electric field $E_{i,y}$ can be written as (see Note S1, Supporting Information, for mathematical derivation)

$$E_{i,y} = \frac{1}{2} E_i (A_l e^{i\varphi_l} - A_w e^{i\varphi_w}) \sin(2\alpha) \mathbf{y} = \begin{cases} \frac{1}{2} E_i \xi |\sin(2\alpha)| e^{i(\Delta+\pi)} \mathbf{y}, & \alpha \in \left[-\frac{\pi}{2}, 0\right) \\ \frac{1}{2} E_i \xi |\sin(2\alpha)| e^{i\Delta} \mathbf{y}, & \alpha \in \left[0, \frac{\pi}{2}\right] \end{cases} \quad (2)$$

where \mathbf{y} denotes the unit vector along the y -direction, ξ and Δ are the modulus and argument of the complex value of $A_l e^{i\varphi_l} - A_w e^{i\varphi_w}$, respectively. The orientation angle, α , represents the included angle between the x axis of laboratory coordinate and l axis, as shown in Figure 1b. In order to generate Airy beams, the amplitude and phase of $E_{i,y}$ should be independently modulated to follow the conditions required by Airy function. Equation (2) clearly indicates the local amplitude of $E_{i,y}$, represented by $1/2 E_i \xi |\sin(2\alpha)|$, solely depends on the orientation angle, α , once the structural parameter of the pillar is fixed. Although the local amplitude of $E_{i,y}$, $1/2 E_i \xi |\sin(2\alpha)|$, will vary with wavelength since ξ is wavelength-dependent, the normalized amplitude, $|\sin(2\alpha)|$, is wavelength-independent and merely determined by the orientation angle, α . Equation (2)

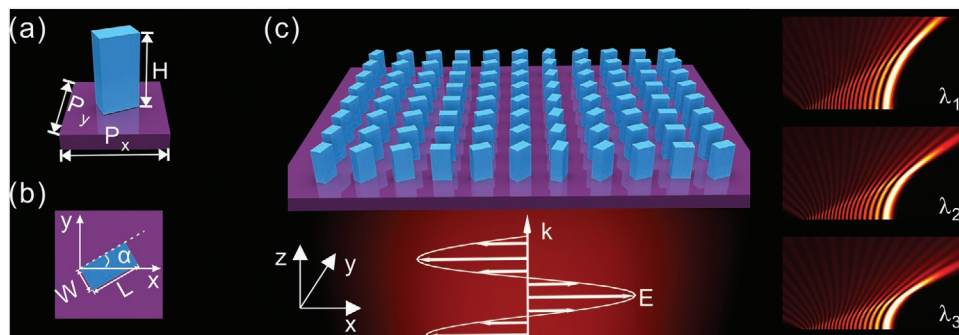


Figure 1. Schematic view of the high-efficiency broadband Airy optical beam generator. a) Side view and b) top view of the subunit. The lengths of three orthometric edges of silicon pillar are denoted as L , W , and H , respectively. The periods are expressed as P_x and P_y , respectively. The orientation angle α is defined as the angle between the x axis of laboratory coordinate and l axis. Two different colors (blue and purple) are only used to distinguish the silicon pillars from the silicon substrate. c) The x -polarized plane waves illuminate the generator from the backside and the broadband Airy beams emerge from the top of metasurfaces.

also indicates that the local phase of $E_{t,y}$ is kept at Δ within $\alpha \in (0, \pi/2)$, but shifts to $\Delta + \pi$ within $\alpha \in (-\pi/2, 0)$, regardless of light wavelength. As a result, $E_{t,y}$ is supposed to follow the amplitude and phase distributions required by Airy function under the x -polarized incidence, so long as the used silicon pillar exhibits birefringence. The rectangle-shaped silicon pillar typically exhibits high birefringence over a wide spectral band and also facilitates conventional nano-fabrication, and hence has been used to serve as the subunit to generate Airy beams in this work. A metasurface Airy beam generator can be constructed by assembling silicon pillars with varied orientation angles along the x -direction (periodic along the y -direction) as schematically shown in Figure 1c. Once the corresponding local amplitude and phase distributions of the transmitted $E_{t,y}$ are designed to follow the Airy function, the Airy beams are expected to be generated from the top of the meta-device that is backside-illuminated by an x -polarized beam.

Transmission efficiency is crucial for transmissive meta-devices and is directly related to the working efficiency of the individual subunit. To explore high-efficiency broadband Airy beam generators, we optimize the silicon pillar to maximize the transmission amplitude of $E_{t,y}$, $1/2E_t\xi|\sin(2\alpha)|$. Simulation results by finite difference time domain (FDTD) method with commercial software Lumerical FDTD Solutions in Figure 2a show the dependence of ξ on H for different W as L is fixed at $0.41 \mu\text{m}$. We can obtain approximate transmission amplitudes along the l and w polarization directions for the silicon pillars, that is, $A_l \approx A_w$. In this case, the maximum value of ξ occurs as

the difference between ϕ_l and ϕ_w approaches π , that is., $t_l \approx -t_w$. To achieve the highest transmission efficiency of the meta-device, one needs to avoid using those geometrical parameters that correspond to the minimum transmission efficiency, associating with the difference between ϕ_l and ϕ_w around 0. Comparatively, the geometrical parameters with $W = 0.2 \mu\text{m}$ and $L = 0.41 \mu\text{m}$ can achieve the largest ξ (3.2) with $H = 0.9 \mu\text{m}$, which is much lower than those heights required for achieving the highest transmission efficiency with other geometrical parameters ($W = 0.1$ and $0.3 \mu\text{m}$). When W is further increased to $0.4 \mu\text{m}$, ξ is always a small value even if H approaches $5 \mu\text{m}$ as t_l is almost equal to t_w . To reduce the fabrication complexity, a thinner and wider silicon pillar is preferred. With $H = 0.9 \mu\text{m}$, the dependence of ξ on W and L is depicted in Figure 2b. It can be seen that the cross-sectional parameters of $W = 0.2 \mu\text{m}$ and $L = 0.41 \mu\text{m}$ will guarantee a high transmission efficiency. By taking the fabrication and transmission efficiency into consideration, $W = 0.2 \mu\text{m}$, $L = 0.41 \mu\text{m}$, and $H = 0.9 \mu\text{m}$ are finally chosen to implement the design and fabrication. The simulation results in Figure 2c,d clearly reveal that the transmission phase and amplitude of $E_{t,y}$ can be modulated over a wide wavelength range by tuning α . The transmission phase experiences a π phase shift between $\alpha \in (-\pi/2, 0)$ and $\alpha \in (0, \pi/2)$ within the wavelength range of interest (Figure 2c). The absolute amplitude distributions versus α are different for different wavelengths, but the normalized amplitude distributions for different wavelengths are almost overlapped (Figure 2d), which means normalized amplitude is wavelength-independent and

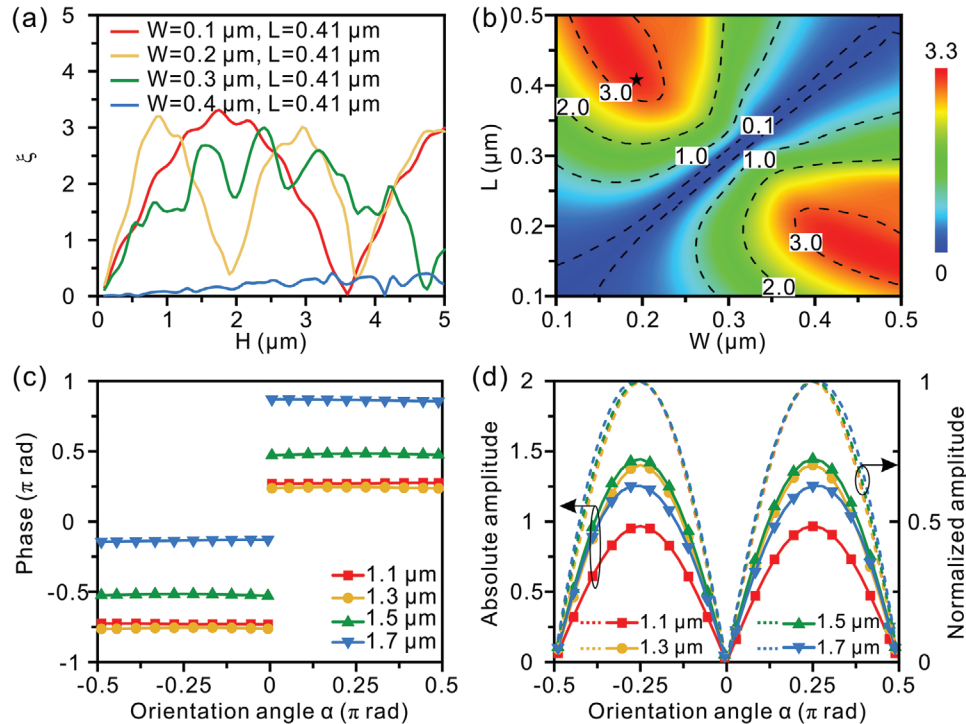


Figure 2. The amplitude and phase response of a rectangle-shaped silicon pillar under the x -polarized incidence. a) ξ versus H for different W with a fixed L of $0.41 \mu\text{m}$ at $\lambda = 1.5 \mu\text{m}$. b) ξ as a function of L and W with $H = 0.9 \mu\text{m}$ at $\lambda = 1.5 \mu\text{m}$. c) The phase and d) amplitude response of $E_{t,y}$ versus α with different wavelengths upon x -polarized incidences. The solid and dashed lines in (d) stand for the absolute and normalized transmission amplitudes, respectively. In the simulations, periodic boundary conditions are employed in the x - and y -directions, and perfectly matched layer (PML) absorption boundary condition is applied in the z -direction.

merely determined by α . For each wavelength, $1/2E_i\xi$ is the same for pillars with different orientation angles. Consequently, the absolute amplitude is proportional to the normalized amplitude $|\sin(2\alpha)|$. For the following design of Airy beam generator, one merely needs to tune the value of α to satisfy the Airy function, and the resultant amplitude distributions can follow the Airy functions over a wide spectral band, since the normalized amplitude, $|\sin(2\alpha)|$, is the same, regardless of light wavelength. In addition, the absolute transmission amplitude of $E_{t,y}$ has its maximum value at the pre-designed wavelength of $1.5\ \mu\text{m}$, but gradually decreases as light wavelength deviates from the pre-designed wavelength.

2.2. Design, Fabrication, and Measurement of Airy Beam Generator

The silicon pillars meet all the conditions to build a high-efficiency and broadband Airy beam. By spatially arranging the silicon pillars with varied orientation angles α along the x -direction, the transmission amplitude and phase distributions of $E_{t,y}$ can be tailored to satisfy the initial envelope of the Airy beam under x -polarized incidence. The electric field envelope of a finite energy 1D Airy beam is described as^[46]

$$U(\sigma, \gamma) = A \cdot \text{Ai}\left[\gamma - \left(\frac{\sigma}{2}\right)^2 + i(a\sigma)\right] \times \exp\left[a\gamma + j\left(\frac{\gamma\sigma}{2}\right) - \left(\frac{a\sigma^2}{2}\right) + i\left(\frac{a^2\sigma}{2}\right) - i\left(\frac{\sigma^3}{12}\right) \right] \quad (3)$$

where A and Ai stand for the amplitude coefficient and Airy function, respectively, and the exponential term indicates the

decaying feature with a being decay factor. $\gamma = (x - x_0)/\delta$ is a normalized dimensionless transverse coordinate, where x is the real laboratory coordinate, x_0 is a translation parameter of coordinate for normalization, and δ is a scale factor. The parameter $\sigma = z/(k_0\delta^2)$ is the propagation length normalized with Rayleigh distance, where k_0 is the propagation constant in vacuum. According to Equation (3), the initial field envelope of the Airy beam can be simplified as

$$U_0(x) = U(0, x) = A \cdot \text{Ai}(\gamma) \exp(a\gamma) \quad (4)$$

under the condition $\delta = 0$. Consider that U_0 is a real-value function, presenting alternatively negative and positive values. This can be realized by controlling the orientation angle, α , of the silicon pillar to generate the required amplitude and phase, in which a phase modulation of Δ and $\Delta + \pi$ is provided. To make the designed Airy beam generator work over a wide spectral band, λ should be taken into account in Equation (4), which yields

$$U_0(\lambda, x) = A(\lambda) \cdot \text{Ai}(\gamma) \exp(a\gamma) \quad (5)$$

In order to attain the maximum transmission efficiency for the Airy beam generator at the designed central wavelength λ_0 , $A(\lambda_0)$ should be set to enable $|U_0(\lambda_0, x)|_{\text{max}} = 1/2\xi(\lambda_0)E_i$. Here, we set $A(\lambda_0) = 1.6$ at $\lambda_0 = 1.5\ \mu\text{m}$, $a = 0.001$, $\delta = P/0.3$, and $x_0 = 42.3\ \mu\text{m}$ to implement the design. The initial field envelope of Airy beam, $U_0(\lambda, x)$, is a real value function, whose absolute value and sign vary with the position coordinate x , as shown in Figure 3a. According to Equation (2), the absolute value of amplitude of $U_0(\lambda, x)$ is decided by the absolute value of the orientation angle, and the sign of $U_0(\lambda, x)$ is determined by

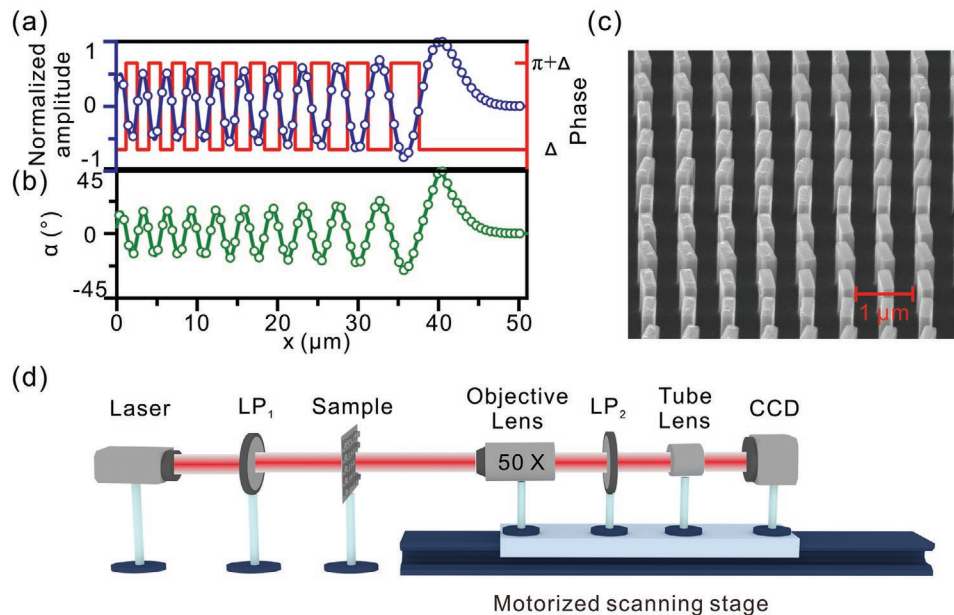


Figure 3. Design, fabrication, and measurement setup of the Airy beam. a) The initial field envelope of the Airy beam at $z = 0$. The blue line is the normalized amplitude profile given by ideal Airy function and the blue hollow circles represent the normalized amplitude distributions given by the designed silicon pillars. The red line stands for the phase profile. b) The orientation angles of silicon nanopillars versus x , where the green hollow circles represent the orientation angle distributions of the sampled silicon pillars. c) SEM image of partial sample for 1D Airy beam generator, where the scale is marked. d) Home-made experimental setup for measurement.

the sign of α . The dependence of α on x is depicted in Figure 3b. 84 subunits with meticulously designed orientation angle α are arranged along the x -direction, while they are assumed to be uniform and infinitely long along the y -direction. The orientation angle α versus position coordinate along the x -direction is numerically listed in Table S1 of Note S2, Supporting Information. The sampling amplitude profile (blue hollow circles in Figure 3a) provided by silicon pillars agrees well with the ideal Airy function. It should be noted that, once a pair of α is chosen: one is within $(0, \pi/2]$ and the other is within $(-\pi/2, 0]$, the associated phase difference will be constantly kept at π . In this case, one can flexibly modulate the transmission amplitude to cover 0 to 1 by changing α . The scheme herein does not decrease the feasibility of device design.

For sample fabrication, the silicon pillars were deeply etched into a 500- μm -thick double-side polished crystalline silicon wafer. A positive photoresist (ZEP520) layer with a thickness of 0.4 μm was spin-coated onto the silicon wafer and baked in oven at 180 degrees for one min. Afterward, the desired patterns were defined on the photoresist layer by electron beam lithography with JEOL JBX6300fs at an acceleration voltage of 100 keV. The development is carried out with amyl acetate solution for 65 s at room temperature, which was followed by ICP-RIE process and O_2 plasma for cleaning the sample. Figure 3c shows the scanning electron microscope (SEM) image of the partial sample for generating Airy beams. The experimental setup is schematically shown in Figure 3d. The sample is backside-illuminated

by a super-continuous white laser (NKT Photonics SuperK EXTREME EXR-15 with the operation wavelength ranging from 1.1 to 1.7 μm) through a fiber collimator lens. The incident light is filtrated with x -polarized linear polarizer (LP₁, Thorlabs LPNIR100-MP) and then an orthorhombic polarizer (LP₂, Thorlabs LPNIR100-MP) was adopted to make y -polarized light transmitted. By means of the combination of a near-infrared objective lens (Mitutoyo MY50X-825, NA = 0.42, 50 \times) and a tube lens (Thorlabs TL200-3P, $f = 200$ mm), the light field is collected by a charge coupled device (CCD) camera (Xenics Bobcat-640-Gige-298) (see more details about measurement in Note S3, Supporting Information).

The simulated and measured field intensity distributions of $|E_y|^2$ in **Figure 4** clearly reveals the generation of Airy beams over a wide spectral band from 1.1 to 1.7 μm under x -polarized incidence. The simulated and experimental results are basically consistent with each other. More details on the simulated and measured electric field intensity distributions at other wavelengths can be found in Figures S3 and S4, Supporting Information. The experimental results show some minor deviation due to fabrication and measurement errors. The parameters of the fabricated sample have some difference with the pre-designed parameters. The measurement errors are probably attributed to the fact that the incident light is not vertical to the metasurface surface. It is worth emphasizing that, although the broadband generation of Airy beams is enabled, the spatial field distributions for different wavelengths are not overlapped.

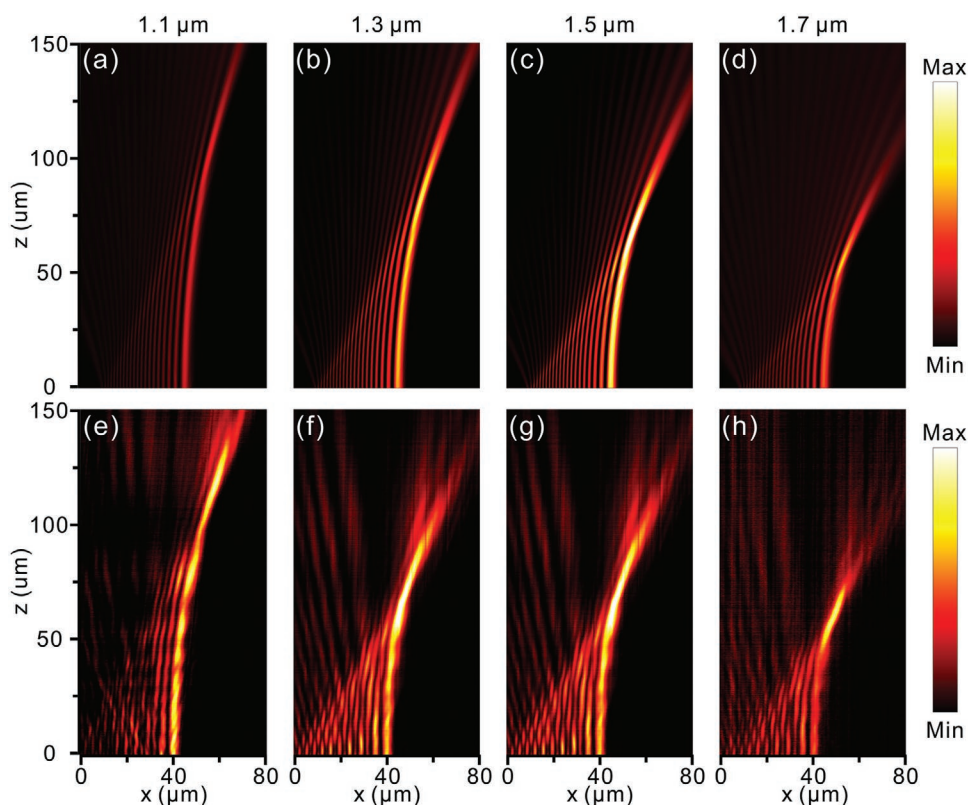


Figure 4. Experimental demonstration of Airy beam generation. The a–d) simulated and e–h) experimental $|E_y|^2$ field intensity distributions at a,e) 1.1, b,f) 1.3, c,g) 1.5, and d,h) 1.7 μm . In the FDTD simulations, the y -direction adopts periodic boundary condition, while PML absorption boundary conditions are employed in the x - and z -directions.

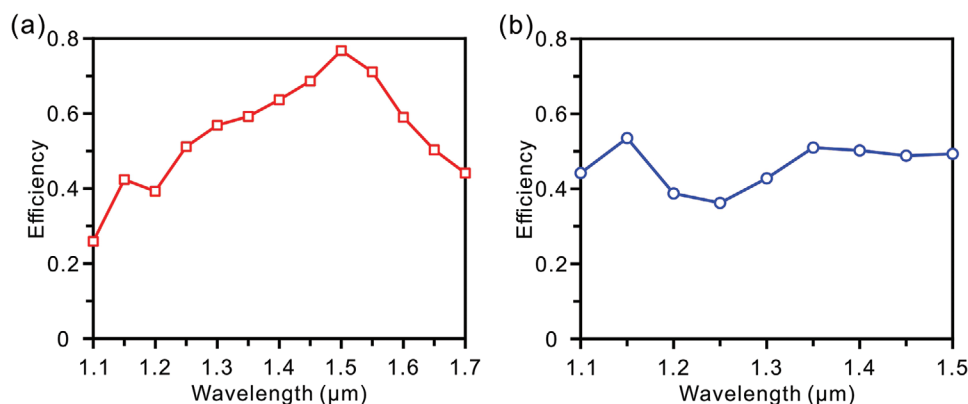


Figure 5. a) The simulated and b) experimental transmission efficiency versus light wavelength.

The transmission efficiency of Airy beam is defined as the ratio of the maximum electric field intensity of Airy beam to the intensity of incident light waves.^[42,49,50] The simulation results indicate the transmission efficiency first increases with light wavelength and reaches the maximum value of 76.8% at 1.5 μm (Figure 5a). This is well consistent with our design, where the pre-designed subunit has the maximum transmission amplitude at 1.5 μm. However, the measured results do not present the maximum efficiency at 1.5 μm, and the measured efficiency above 1.5 μm is inaccurate, which therefore has not been shown in Figure 5b. The reason that causes inaccurate data at long wavelengths mainly comes from the reduction of laser power and quantum efficiency of CCD. This will make the signal-noise-ratio decrease sharply, associated with inaccurate transmission efficiency. The measured transmission efficiencies are higher than the simulated values within 1.1–1.2 μm due to the fact that the reduction of the laser power results in lower signal to noise ratios at short wavelengths (see more details in Note S3, Supporting Information). The wavelength-dependent transmission efficiency is understandable as the silicon pillars exhibit wavelength-dependent birefringence.

The three key characteristics of Airy beams that differ from other dynamically controlled beams are the non-diffracting, self-acceleration behavior, and self-healing properties in the absence of any external potential. The diffraction-free and self-acceleration properties can be assessed by full width half-maximum (FWHM) and deflection offset (x_d) of the main lobe. According to the paraxial approximation, the theoretical value of the deflection offset can be expressed as^[51]

$$x_d \approx \lambda^2 z^2 / (16\pi^2 \delta^3) \quad (6)$$

The three performances are verified by numerical simulation and experiment in Figure 6. More details at other wavelengths are provided in Figure S5 of Note S4 in the Supporting Information. Figure 6a–d presents the FWHMs of the main lobe for the four wavelengths, which clearly shows the FWHMs oscillate around the pre-designed value of 3.3 μm (green solid line). The non-diffracting region defined as the FWHM is below 1.5 times of the pre-designed values (green dashed line). The diffraction effects gradually take dominance if the beams depart from the non-diffraction region. The propagation distances, associated with the FWHM being 1.5 times of the pre-designed values, are 154, 123,

97, and 82 μm at 1.1, 1.3, 1.5 and 1.7 μm, respectively. Afterward, the quality of beams gradually degrades with propagation. The deflection offsets versus the propagation distance are exhibited in Figure 6e–h, showing some difference among simulation, experiment, and theoretical values retrieved from Equation (6). In both of the FDTD simulation and optical measurements, the used light source is larger than the device size. The difference between the simulated/measured results and theoretical values arise from a finite number of silicon pillars used in practice, and hence the provided amplitude and phase distributions do not fully fulfill the ideal Airy function. The difference between simulated and experimental results mainly come from the fabrication errors. The fabricated samples inevitably have to be slightly inconsistent with the pre-designed devices. It should be noted here, although the deflection offsets for different wavelengths are different, the proposal can still find many potential applications, including imaging,^[52] micromachining of curved profiles,^[53] communication,^[3] where the overlapped spatial field intensity distributions for different wavelengths are not a prerequisite. In order to validate the self-healing performance, a scatter block made of a perfect electric conductor block with 1 μm, 0.6 μm in size, is placed on the travelling path of the main lobe. It is apparent from Figure 6i–l that nearly intact Airy beams recover as the scatter block locates at $(x, z) = (40 \mu\text{m}, 14 \mu\text{m})$. More details on the self-healing characteristics at other wavelengths can be found in Figure S5 of Note S4 in Supporting Information. It is also worth noting, although we have merely presented the performance of the Airy beams within 1.1–1.7 μm in the experiment, the proposal actually can work beyond this wavelength range (see the simulated results below 1.1 and above 1.7 μm in Note S5, Supporting Information). Finally, we emphasize that, the designed Airy beam generator can also work under γ -polarized incidence, and the generated Airy beam is x -polarized (see Notes S1 and S6, Supporting Information).

3. Conclusion

In summary, we have proposed a design strategy of building high-efficiency broadband Airy beam generators in the optical domain. By utilization of the high birefringence and transmission efficiency of silicon metasurfaces, the local amplitude and phase of transmitted light can be simultaneously modulated to satisfy the Airy function by controlling the orientation angle of

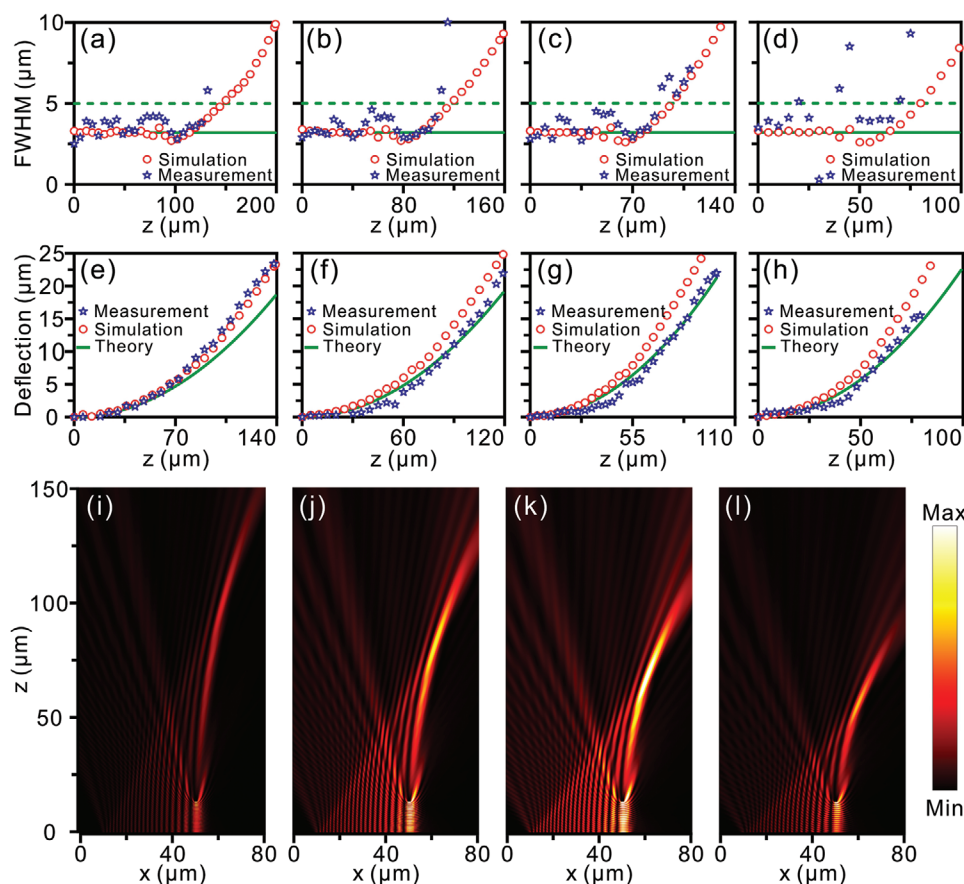


Figure 6. The optical characteristics of Airy beams. The dependence of a–d) FWHM and e–h) deflection offset on the propagation distance at a,e) 1.1, b,f) 1.3, c,g) 1.5, and d,h) 1.7 μm . i–l) The numerical simulation verification of self-healing properties at i) 1.1, j) 1.3, k) 1.5, and l) 1.7 μm .

silicon pillars, regardless of the incidence wavelength. High-efficiency Airy beams were experimentally observed over an ultra-wide spectral band ranging from 1.1 to 1.7 μm , which is the widest operation bandwidth achieved for Airy beams in the optical domain with metasurfaces to date. These results may pave a meaningful step toward exploration of practical applications with optical metasurfaces, such as optical micromanipulation, chip-scaled signal processing, and microscopy.

Supporting Information

Supporting Information is available from the Wiley Online Library or from the author.

Acknowledgements

Z.J., J.W., and L.S. contributed equally to this work. This work was supported by the National Key R&D Program of China (Grant Nos. 2018YFB2200200 and 2018YFA0701800), the National Natural Science Foundation of China (Grant Nos. 11674118, 12074137, 81701745, 61775140 and 61875225), Shanghai Municipal Science and Technology Commission Innovation Action Plan (Grant No. 18DZ1100400) and State Key Laboratory of Advanced Technology for Materials Synthesis and Processing (Wuhan University of Technology).

Conflict of Interest

The authors declare no conflict of interest.

Keywords

Airy optical beams, broadband, high efficiency, metasurfaces

Received: July 29, 2020

Revised: October 7, 2020

Published online:

- [1] H. Cheng, W. Zang, W. Zhou, J. Tian, *Opt. Express* **2010**, *18*, 20384.
- [2] P. Zhang, J. Prakash, Z. Zhang, M. S. Mills, N. K. Efremidis, D. N. Christodoulides, Z. Chen, *Opt. Lett.* **2011**, *36*, 2883.
- [3] P. Rose, F. Diebel, M. Boguslawski, C. Denz, *Appl. Phys. Lett.* **2013**, *102*, 101101.
- [4] N. Wiersma, N. Marsal, M. Sciamanna, D. Wolfersberger, *Opt. Lett.* **2014**, *39*, 5997.
- [5] S. Jia, J. C. Vaughan, X. Zhuang, *Nat. Photonics* **2014**, *8*, 302.
- [6] X.-J. Tan, C. Kong, Y.-X. Ren, C. S. W. Lai, K. K. Tsia, K. K. Y. Wong, *Opt. Lett.* **2019**, *44*, 391.
- [7] P. Polynkin, M. Kolesik, J. V. Moloney, G. A. Siviloglou, D. N. Christodoulides, *Science* **2009**, *324*, 229.

- [8] D. Abdollahpour, S. Sunstov, D. G. Papazoglou, S. Tzortzakis, *Phys. Rev. Lett.* **2010**, *105*, 253901.
- [9] P. Panagiotopoulos, D. G. Papazoglou, A. Couairon, S. Tzortzakis, *Nat. Commun.* **2013**, *4*, 2622.
- [10] J.-X. Li, W.-P. Zang, J.-G. Tian, *Opt. Lett.* **2010**, *35*, 3258.
- [11] J.-X. Li, X.-L. Fan, W.-P. Zang, J.-G. Tian, *Opt. Lett.* **2011**, *36*, 648.
- [12] G. A. Siviloglou, D. N. Christodoulides, *Opt. Lett.* **2007**, *32*, 979.
- [13] Z. Ren, Q. Wu, Y. Shi, C. Chen, J. Wu, H. Wang, *Opt. Express* **2014**, *22*, 15154.
- [14] D. Luo, H. T. Dai, X. W. Sun, *Opt. Express* **2013**, *21*, 31318.
- [15] B.-Y. Wei, P. Chen, W. Hu, W. Ji, L.-Y. Zheng, S.-J. Ge, Y. Ming, V. Chigrinov, Y.-Q. Lu, *Sci. Rep.* **2015**, *5*, 17484.
- [16] B.-Y. Wei, S. Liu, P. Chen, S.-X. Qi, Y. Zhang, W. Hu, Y.-Q. Lu, J.-L. Zhao, *Appl. Phys. Lett.* **2018**, *112*, 121101.
- [17] B. Yalozay, B. Soyulu, S. Akturk, *J. Opt. Soc. Am. A* **2010**, *27*, 2344.
- [18] R. Cao, Y. Yang, J. Wang, J. Bu, M. Wang, X. C. Yuan, *Appl. Phys. Lett.* **2011**, *99*, 261106.
- [19] L. Niu, C. Liu, Q. Wu, K. Wang, Z. Yang, J. Liu, *IEEE Photonics J.* **2017**, *9*, 5900407.
- [20] Z. Miao, Z. Hao, B. Jin, Z. N. Chen, *IEEE Trans. Antennas Propag.* **2020**, *68*, 1503.
- [21] P. C. Wu, W.-Y. Tsai, W. T. Chen, Y.-W. Huang, T.-Y. Chen, J.-W. Chen, C. Y. Liao, C. H. Chu, G. Sun, D. P. Tsai, *Nano Lett.* **2017**, *17*, 445.
- [22] P. C. Wu, J.-W. Chen, C.-W. Yin, Y.-C. Lai, T. L. Chung, C. Y. Liao, B. H. Chen, K.-W. Lee, C.-J. Chuang, C.-M. Wang, D. P. Tsai, *ACS Photonics* **2018**, *5*, 2568.
- [23] H. Zhu, S. Chen, J. Wen, J. Wang, L. Chen, *Opt. Lett.* **2019**, *44*, 5764.
- [24] Z. Wu, Y. Ra'di, A. Grbic, *Phys. Rev. X* **2019**, *9*, 011036.
- [25] S. Wang, P. C. Wu, V. C. Su, Y. C. Lai, C. Hung Chu, J. W. Chen, S. H. Lu, J. Chen, B. Xu, C. H. Kuan, T. Li, S. Zhu, D. P. Tsai, *Nat. Commun.* **2017**, *8*, 187.
- [26] S. Wang, P. C. Wu, V.-C. Su, Y.-C. Lai, M.-K. Chen, H. Y. Kuo, B. H. Chen, Y. H. Chen, T.-T. Huang, J.-H. Wang, R.-M. Lin, C.-H. Kuan, T. Li, Z. Wang, S. Zhu, D. P. Tsai, *Nat. Nanotechnol.* **2018**, *13*, 227.
- [27] T. Yang, H. Lin, B. Jia, *Front. Optoelectron.* **2018**, *11*, 2.
- [28] W. T. Chen, A. Y. Zhu, J. Sisler, Z. Bharwani, F. Capasso, *Nat. Commun.* **2019**, *10*, 355.
- [29] C. Chen, W. Song, J.-W. Chen, J.-H. Wang, Y. H. Chen, B. Xu, M.-K. Chen, H. Li, B. Fang, J. Chen, H. Y. Kuo, S. Wang, D. P. Tsai, S. Zhu, T. Li, *Light: Sci. Appl.* **2019**, *8*, 99.
- [30] X. Yin, H. Zhu, H. Guo, M. Deng, T. Xu, Z. Gong, X. Li, Z. H. Hang, C. Wu, H. Li, S. Chen, L. Zhou, L. Chen, *Laser Photonics Rev.* **2019**, *13*, 1800081.
- [31] Y.-W. Huang, W. T. Chen, W.-Y. Tsai, P. C. Wu, C.-M. Wang, G. Sun, D. P. Tsai, *Nano Lett.* **2015**, *15*, 3122.
- [32] J. Guo, T. Wang, H. Zhao, X. Wang, S. Feng, P. Han, W. Sun, J. Ye, G. Situ, H.-T. Chen, Y. Zhang, *Adv. Opt. Mater.* **2019**, *7*, 1801696.
- [33] H. Ren, G. Briere, X. Fang, P. Ni, R. Sawant, S. Héron, S. Chenot, S. Vézian, B. Damilano, V. Brändli, S. A. Maier, P. Genevet, *Nat. Commun.* **2019**, *10*, 2986.
- [34] Y. Yang, L. Jing, B. Zheng, R. Hao, W. Yin, E. Li, C. M. Soukoulis, H. Chen, *Adv. Mater.* **2016**, *28*, 6866.
- [35] H. Chu, Q. Li, B. Liu, J. Luo, S. Sun, Z. H. Hang, L. Zhou, Y. Lai, *Light: Sci. Appl.* **2018**, *7*, 50.
- [36] D. Hakobyan, H. Magallanes, G. Seniutinas, S. Juodkazis, E. Brasselet, *Adv. Opt. Mater.* **2016**, *4*, 306.
- [37] L. Zhu, J. Wang, *Front. Optoelectron.* **2019**, *12*, 52.
- [38] C. Wan, G. Rui, J. Chen, Q. Zhan, *Front. Optoelectron.* **2019**, *12*, 88.
- [39] H. Sroor, Y.-W. Huang, B. Sephton, D. Naidoo, A. Vallés, V. Ginis, C.-W. Qiu, A. Ambrosio, F. Capasso, A. Forbes, *Nat. Photonics* **2020**, *14*, 498.
- [40] A. Minovich, A. E. Klein, N. Janunts, T. Pertsch, D. N. Neshev, Y. S. Kivshar, *Phys. Rev. Lett.* **2011**, *107*, 116802.
- [41] Z. Li, H. Cheng, Z. Liu, S. Chen, J. Tian, *Adv. Opt. Mater.* **2016**, *4*, 1230.
- [42] E.-Y. Song, G.-Y. Lee, H. Park, K. Lee, J. Kim, J. Hong, H. Kim, B. Lee, *Adv. Opt. Mater.* **2017**, *5*, 1601028.
- [43] S. Wang, X. Wang, Y. Zhang, *Opt. Express* **2017**, *25*, 23589.
- [44] X. Yin, L. Chen, X. Li, *Opt. Express* **2018**, *26*, 23251.
- [45] T. Wang, G. Zhai, R. Xie, S. Zhu, J. Gao, S. An, B. Zheng, H. Li, Y. Liu, H. Zhang, J. Ding, *Adv. Theory Simul.* **2019**, *2*, 1900071.
- [46] Q. Fan, D. Wang, P. Huo, Z. Zhang, Y. Liang, T. Xu, *Opt. Express* **2017**, *25*, 9285.
- [47] Q. Fan, W. Zhu, Y. Liang, P. Huo, C. Zhang, A. Agrawal, K. Huang, X. Luo, Y. Lu, C. Qiu, H. J. Lezec, T. Xu, *Nano Lett.* **2019**, *19*, 1158.
- [48] B. Yu, J. Wen, L. Chen, L. Zhang, Y. Fan, B. Dai, S. Kanwal, D. Lei, D. Zhang, *Photonics Res.* **2020**, *8*, 1148.
- [49] H. Li, W. Hao, X. Yin, S. Chen, L. Chen, *Adv. Opt. Mater.* **2019**, *7*, 1900493.
- [50] W. Hao, M. Deng, S. Chen, L. Chen, *Phys. Rev. Appl.* **2019**, *11*, 054012.
- [51] G. A. Siviloglou, J. Broky, A. Dogariu, D. N. Christodoulides, *Phys. Rev. Lett.* **2007**, *99*, 213901.
- [52] Z. Cai, X. Qi, D. Pan, S. Ji, J. Ni, Z. Lao, C. Xin, J. Li, Y. Hu, D. Wu, J. Chu, *Photonics Res.* **2020**, *8*, 875.
- [53] A. Mathis, F. Courvoisier, L. Froehly, L. Furfaro, M. Jacquot, P. A. Lacourt, J. M. Dudley, *Appl. Phys. Lett.* **2012**, *101*, 071110.